The International Journal of Advanced Manufacturing Technology (2018) 95:4265–4277
https://doi.org/10.1007/s00170-017-1526-0

ORIGINAL ARTICLE

Sheet metal anisotropy and optimal non-round blank design in high-speed multi-step forming of AA3104-H19 aluminium alloy can body

Wencheng Liu[1] · **Bernard K Chen**[1]

Received: 20 September 2017 / Accepted: 18 December 2017 / Published online: 9 January 2018

Abstract

A new anisotropic yield function which accurately describes the complex anisotropy of aluminium alloy sheet metal is proposed in this paper. A non-linear least square method is used to determine the coefficients of this yield function based on the experimental results. By employing the back-Euler stress integration algorithm, this anisotropic constitutive model has been successfully implemented in commercial FEM software ABAQUS via user material subroutine UMAT to predict earing profile of AA3104-H19 deep-drawn and redrawn cups. Good agreement was found in the predicted earing profiles and those obtained in experimental deep-drawn and redrawn cups. The FE model was used in an iteration optimisation process to determine the optimal shape of non-round blanks to obtain the ear-free deep-redrawn cups, and non-round tooling was designed accordingly. Results showed the height of the ears is significantly reduced in the cup formed using this non-round blank compared with that of a conventional round blank which is important for smooth running of high-speed multi-step forming of aluminium can body.

Keywords Yield function · Non-round blank · Anisotropy · Ear-free

1 Introduction

In metal packaging industry, the two-piece aluminium beverage can which consists of the can body and the can end is manufactured in a multi-step high-speed forming process.

Figure 1 shows a typical manufacturing process of the standard 330-ml can body. The first stage of can body production is carried out in a “Cupper” in which two operations are performed: blanking and deep drawing. In this stage, blanks are cut from large coils of cold-rolled aluminium sheet with a thickness about 0.25–0.30 mm, then a ram presses them through draw die to form cups. Subsequent operations—redrawing, ironing, dome-forming, and trimming—take place in the “Bodymaker”. Firstly, a sleeve holds the cup precisely in place, and a punch is lowered swiftly into the redraw die to reduce the diameter and increase the height of this cup. Then, the punch continues to push the redrawn cup against three rings called ironing rings, which reduces the thickness of the wall and increases the height of the cup. This is done in one continuous punch stroke which takes only one fifth of a second to complete. At the end of the stroke, another punch presses up against the base of the cup to form the reverse dome. Finally, a trimmer is employed to remove the ears at the top of the can to a set cup height (Fig. 2). The cans are now ready to be clean, surface coated, decorated, and filled.

AA3104-H19 aluminium alloy satisfies both strength and formability requirements for beverage can bodies; however, the resultant earing arising from the crystallographic texture of rolled aluminium sheet may adversely affect the smooth production of large can volumes, estimated at 100 billion annually in North America alone [1]. Deep drawing a cup from a round blank punched off a flat-rolled sheet gives rise to earing profile at the top of the can wall which further develops through the subsequent redrawing and ironing in the Bodymaker. Excessive earing not only requires extra material to be trimmed from the top of the can but directly

---

✉ Wencheng Liu
Wencheng.Liu@monash.edu

[1] Department of Mechanical and Aerospace Engineering, Monash University, Melbourne, Victoria 3800, Australia

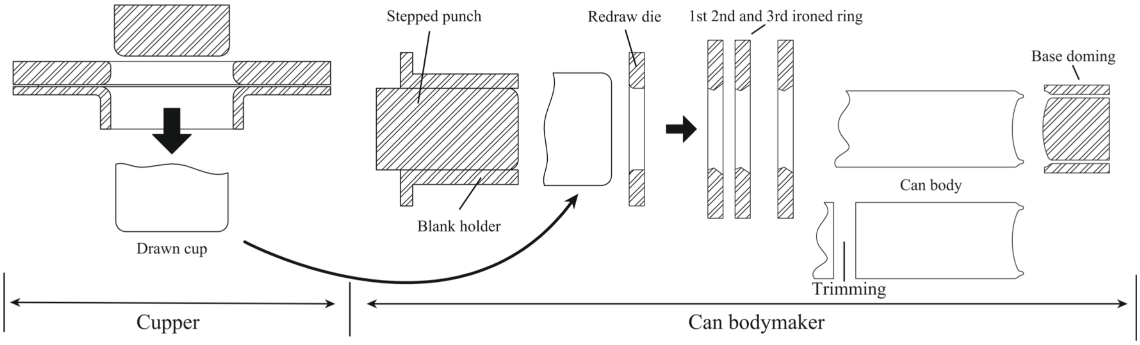

Fig. 1 Manufacturing process of standard aluminium beverage can (“Cupper” and “Bodymaker”)

contribute to jams in extremely high-speed forming process leading to machine down time and loss of productivity.

In the past, the starting material for can bodies was round blanks. Understanding of the evolution of microstructure during hot rolling and cold rolling was critical to reducing sheet anisotropy and cup earing. Extensive research were undertaken in recrystallisation, formation of cube, and rolling textures to control the sheet planar anisotropy in the rolling process and annealing process [2–6]. Thiruvarudchelvan and Loh [7] employed extra annealing process before the drawing process to minimise earing. However, it was impossible to completely eliminate mechanical anisotropy through control of microstructure which led to the development of non-round blanks for aluminium beverage cans to further reduce the magnitude of earing in deep-drawn cans.

The profile of the non-round blank was designed to compensate for typical peaks and troughs of earing around the top of the can so that the final deep-drawn and ironed cup appears flat at the top. Analytical and numerical methods [8–17] were employed to analyse various non-round blank shapes and the resultant earing. Varying levels of success were achieved. For example, previous work based on analytical algorithms and Barlat-Lian yield function [18] was able to predict four ears around the circumference of the cup. Most ignored anisotropic plastic flow in the forming process and others directly inversed the earing profile (obtained from a round blank) to determine the non-round blank profile. However, these methods had limitations since can body stock AA3104-H19 develops up to eight ears in the forming process. Engler [19] proposed a texture-based polycrystal-plasticity model to predict earing upon deep drawing and investigated the use of non-round blank profiles which were derived from directly inversing the earing profile formed with a round blank. Although the outcome was beneficial, the inverse profile did not lead to ear-free cups. In addition, most previous work focussed on the first deep drawing step of the can making process, but neglected earing that develops in subsequent redrawing and ironing processes. Although ironing tends even out the level earing, the analysis should include redrawing since excessive earing is very likely to cause the jams in the ironing rings [20].

Fig. 2 Experimental samples of untrimmed and trimmed can bodies

In this study, a new yield function is proposed in which parameters required to better describe anisotropy of the AA3104-H19 were obtained using a series of the uniaxial and equibiaxial tension tests. This work builds on convex yield functions, established on the concept of the multiple linear transformations of the stress deviator to describe the complicated anisotropy of the aluminium alloys [21–26]. Greater accuracy is achieved through more extensive use of linear transformations in the yield function. Implementation of this yield function in FE code is described in detail in the following sections. The FE model was then used to predict the multi-step forming process including deep drawing and redrawing to accurately predict the earing profile after each forming process. This model was validated with experimental results and applied to achieve the ear-free production of redrawn aluminium cup. The results of this work have been applied in industry and have led to the reduction of probability of jams happening in forming dies and tooling.

2 Methods

2.1 New anisotropic yield function

The Yld2004 yield function based on two linear transformations has been applied to describe the anisotropic plastic yield of aluminium alloy[23]:

$$\psi_1(\sigma) = \sum_{i=1}^{3}\sum_{j=1}^{3}\left[\left|\tilde{S}_i{}' - \tilde{S}_j{}''\right|^m\right] = 4\sigma_e^m \tag{1}$$

However, the anisotropic properties of the AA3104-H19 aluminium alloy are fairly complicated and required more than two linear transformations to accurately describe the earing in deep-drawn cups. Therefore, a new anisotropic yield function in plane stress state was formulated based on the established concept of multiple linear transformations of the stress deviator. The linear transformation is subjected to the constraints (i) that the independence of the response on hydrostatic pressure is preserved and (ii) that orthotropic symmetry is ensured. The operating fourth-order tensor contains free parameters that may be calibrated to experimental data. Four linear transformations were employed in the new yield function to describe the yield surface. The form of this yield function is given by

$$\begin{aligned}\psi_2(\sigma) &= \sum_{i=1}^{3}\sum_{j=1}^{3}\left[\left|\tilde{S}_i{}' - \tilde{S}_j{}''\right|^m\right] + \sum_{i=1}^{3}\left[\left|\tilde{X}_i{}'\right|^m + \left|\tilde{X}_j{}''\right|^m\right] \\ &= \xi\sigma_e^m\end{aligned} \tag{2}$$

where σ_e is the effective stress. The exponent m is 6 and 8 for FCC and BCC materials, respectively. The scalar ξ follows from uniaxial or equibiaxial tension in the isotropic case and can be derived as follows:

$$\xi = (4/3)^m + 6\cdot(2/3)^m + 8\cdot(1/3)^m \tag{3}$$

In plane stress state, the $\tilde{S}_k$ and $\tilde{X}_k$ are the principal values of the transformed stress tensor $\tilde{\mathbf{s}}$ and $\tilde{\mathbf{x}}$ given by

$$\tilde{S}_1, \tilde{S}_2 = \frac{\tilde{s}_{xx} + \tilde{s}_{yy}}{2} \pm \sqrt{\left(\frac{\tilde{s}_{xx} - \tilde{s}_{yy}}{2}\right)^2 + \tilde{s}_{xy}^2},\ \tilde{S}_3 = \tilde{s}_{zz} \tag{4}$$

$$\tilde{X}_1, \tilde{X}_2 = \frac{\tilde{x}_{xx} + \tilde{x}_{yy}}{2} \pm \sqrt{\left(\frac{\tilde{x}_{xx} - \tilde{x}_{yy}}{2}\right)^2 + \tilde{x}_{xy}^2},\ \tilde{X}_3 = \tilde{x}_{zz} \tag{5}$$

The transformed stress tensors $\tilde{\mathbf{s}}$ and $\tilde{\mathbf{x}}$ are obtained by four linear transformations

$$\tilde{\mathbf{s}}' = \boldsymbol{\alpha}'\cdot\mathbf{s} = \boldsymbol{\alpha}'\cdot\mathbf{T}\cdot\boldsymbol{\sigma} \tag{6}$$

$$\tilde{\mathbf{s}}'' = \boldsymbol{\alpha}''\cdot\mathbf{s} = \boldsymbol{\alpha}''\cdot\mathbf{T}\cdot\boldsymbol{\sigma} \tag{7}$$

$$\tilde{\mathbf{x}}' = \boldsymbol{\beta}'\cdot\mathbf{x} = \boldsymbol{\beta}'\cdot\mathbf{T}\cdot\boldsymbol{\sigma} \tag{8}$$

$$\tilde{\mathbf{x}}'' = \boldsymbol{\beta}''\cdot\mathbf{x} = \boldsymbol{\beta}''\cdot\mathbf{T}\cdot\boldsymbol{\sigma} \tag{9}$$

where $\boldsymbol{\alpha}'$, $\boldsymbol{\alpha}''$, $\boldsymbol{\beta}'$, and $\boldsymbol{\beta}''$ are the associated linear transformations on the stress deviator which are used to capture the material anisotropy and $\mathbf{T}$ is the constant linear transformation. In plane stress state, they are given by

$$\boldsymbol{\alpha} = \begin{bmatrix} 0 & -\alpha_{12} & -\alpha_{13} & 0 \\ -\alpha_{21} & 0 & -\alpha_{23} & 0 \\ -\alpha_{31} & -\alpha_{32} & 0 & 0 \\ 0 & 0 & 0 & \alpha_{44} \end{bmatrix} \tag{10}$$

$$\boldsymbol{\beta} = \begin{bmatrix} 0 & -\beta_{12} & -\beta_{13} & 0 \\ -\beta_{21} & 0 & -\beta_{23} & 0 \\ -\beta_{31} & -\beta_{32} & 0 & 0 \\ 0 & 0 & 0 & \beta_{44} \end{bmatrix} \tag{11}$$

$$\mathbf{T} = \frac{1}{3}\begin{bmatrix} 2 & -1 & 0 \\ 1 & -2 & 0 \\ 1 & -1 & 0 \\ 0 & 0 & 3 \end{bmatrix} \tag{12}$$

2.2 Determination of coefficients of yield function

In order to accurately determine the anisotropic properties of the aluminium sheet, the uniaxial and equibiaxial tension tests from samples obtained from various directions with respect to the rolling direction were required. The well-known non-linear least-square method Levenberg-Marquardt algorithm was applied to determine the in-plane anisotropic coefficients of the new function curve $f\left(\mathbf{Y}_\varphi^f, \mathbf{r}_\varphi^f, r_b, \boldsymbol{\alpha}', \boldsymbol{\alpha}'', \boldsymbol{\beta}', \boldsymbol{\beta}''\right)$ so that the sum of the squares of the deviations is minimised:

$$\begin{aligned}\hat{R} &= argmin\sum_{i=1}^{n_Y}\left[\mathbf{Y}_\varphi^{exp} - \mathbf{Y}_\varphi^f\right]^2 + argmin\sum_{i=1}^{n_r}\left[\mathbf{r}_\varphi^{exp} - \mathbf{r}_\varphi^f\right]^2 \\ &\quad + min\left[r_b^{exp} - r_b^f\right]\end{aligned} \tag{13}$$

where $\mathbf{Y}_\varphi^{exp}$ and $\mathbf{r}_\varphi^{exp}$ are the directional experimental uniaxial tension yield stress and r-value, respectively. r_b^{exp} is the equibiaxial r-value. The counterparts which are the calculated $\mathbf{Y}_\varphi^f$, $\mathbf{r}_\varphi^f$ and r_b^f of the model are defined as

$$\mathbf{Y}_\varphi^f = \frac{Y_{ref}}{\sigma_e}\ |_{\sigma_\varphi} \tag{14}$$

$$r_b^f = \frac{\frac{\partial\sigma_e}{\partial\sigma_{22}}}{\frac{\partial\sigma_e}{\partial\sigma_{11}}}\ |_{\sigma_b} \tag{15}$$

$$\mathbf{r}_\varphi^f = -\frac{\sin^2\varphi\frac{\partial\sigma_e}{\partial\sigma_{11}} + \cos^2\varphi\frac{\partial\sigma_e}{\partial\sigma_{11}} - \sin\varphi\cos\varphi\frac{\partial\sigma_e}{\partial\sigma_{12}}}{\frac{\partial\sigma_e}{\partial\sigma 11} + \frac{\partial\sigma_e}{\partial\sigma 22}}\ |_{\sigma_\varphi} \tag{16}$$

Table 1 New yield function parameters for the aluminium alloy AA3104-H19 (m=8)

As-rolled AA3104-H19 aluminium alloy sheet metal						
α'_{12}	α'_{13}	α'_{21}	α'_{23}	α'_{31}	α'_{32}	α'_{44}
−0.158955	0.239325	0.203951	0.582336	0.412292	0.530619	1.179920
α''_{12}	α''_{13}	α''_{21}	α''_{23}	α''_{31}	α''_{32}	α''_{44}
−0.601232	1.208809	0.695412	0.251087	−0.323703	0.062360	0.813114
β'_{12}	β'_{13}	β'_{21}	β'_{23}	β'_{31}	β'_{32}	β'_{44}
1.598671	2.328637	0.067186	0.820016	0.732823	1.057809	1.444215
β''_{12}	β''_{13}	β''_{21}	β''_{23}	β''_{31}	β''_{32}	β''_{44}
0.950818	1.376494	2.206390	1.565730	0.538969	0.160378	1.699809

where the uniaxial tension stress tensor $\boldsymbol{\sigma}_\varphi$ and equibiaxial stress tensor $\boldsymbol{\sigma}_b$ are given as

$$\boldsymbol{\sigma}_\varphi = \begin{bmatrix} \sigma_{11} & \sigma_{12} & 0 \\ \sigma_{21} & \sigma_{22} & 0 \\ 0 & 0 & 0 \end{bmatrix} = \begin{bmatrix} Y_\varphi \cos^2\varphi & Y_\varphi \sin\varphi\cos\varphi & 0 \\ Y_\varphi \sin\varphi\cos\varphi & Y_\varphi \sin^2\varphi & 0 \\ 0 & 0 & 0 \end{bmatrix} \tag{17}$$

$$\boldsymbol{\sigma}_b = \begin{bmatrix} \sigma_{11} & 0 & 0 \\ 0 & \sigma_{22} & 0 \\ 0 & 0 & 0 \end{bmatrix} = \begin{bmatrix} Y_b & 0 & 0 \\ 0 & Y_b & 0 \\ 0 & 0 & 0 \end{bmatrix} \tag{18}$$

The experimental uniaxial tension yield stress $\mathbf{Y}_\varphi^{exp}$ and r-value $\mathbf{r}_\varphi^{exp}$ of can body stock (AA3104-H19) are those reported by Aretz et al. [25, 26]. These tension tests were used to generate the 28 parameters of the four linear transformation matrices (Table 1) by using the procedure described above.

Figure 3a, b shows that the material anisotropy of AA3104-H19 is very well described by the new anisotropic yield function which is an important prerequisite for an accurate earing prediction. The variation in r-values shows the good flexibility and is able to describe up to six ears. The yield stress is slightly increasing from the rolling direction (RD) to the transverse direction (TD) which indicates less plastic flow away from the rolling direction.

2.3 Constitutive model for anisotropic sheet metal

In this section, an elastic-plastic constitutive model for plane stress state is presented to describe the anisotropic behaviour of as-rolled sheet metal in forming process of can bodies. The constitutive model with the new anisotropic yield function was implemented in commercial FEM software ABAQUS via user material subroutine UMAT. The flowchart of the constitutive model is shown in Fig. 5. The implemented computational plasticity algorithms rely on small strain assumptions at the discrete level (Gauss points) which are consistent with a corotational approach and the consequent equivalence between the Cauchy stress tensor and the rotated second Piola-Kirchhoff stress tensor. Objective stress rate is based on the Jaumann rate of the Cauchy stress and assumes an additive decomposition of the strain tensor where the total strain increment $\Delta\boldsymbol{\varepsilon}^t$ consists of an elastic $\Delta\boldsymbol{\varepsilon}^e$ and a plastic $\Delta\boldsymbol{\varepsilon}^p$ increment:

$$\Delta\boldsymbol{\varepsilon}^t = \Delta\boldsymbol{\varepsilon}^e + \Delta\boldsymbol{\varepsilon}^p \tag{19}$$

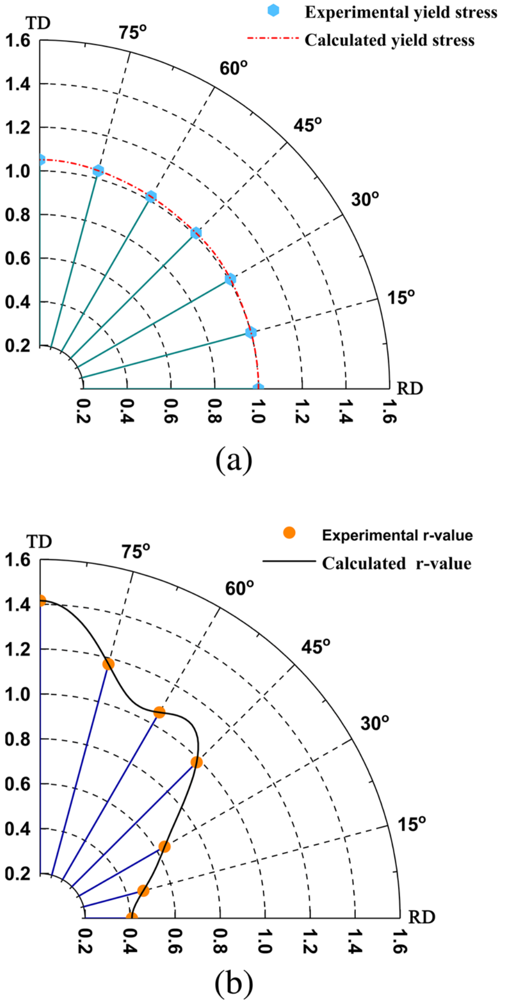

Fig. 3 Calculated **a** normalised uniaxial yield stress and **b** r-value for the aluminium alloy AA3104-H19 using the new yield function shown from rolling direction (RD) to transverse direction (TD)

The elastic behaviour is assumed as isotropic and linear, the increment of the elastic stress following the Hooke's law,

$$\Delta\boldsymbol{\sigma} = \mathbf{D} : (\Delta\boldsymbol{\varepsilon}^t - \Delta\boldsymbol{\varepsilon}^p) \tag{20}$$

where $\mathbf{D}$ is the elastic stiffness matrix. The elastic predictor stress $\boldsymbol{\sigma}_B$ (linear orthotropic) is determined:

$$\boldsymbol{\sigma}_{\boldsymbol{B}} = \boldsymbol{\sigma} + \mathbf{D} : \Delta\boldsymbol{\varepsilon}^t \tag{21}$$

The yield criterion determined by Yld2004 and new yield function, respectively, as

$$f_1 = \psi_1(\boldsymbol{\sigma}_B) - 4\sigma_0^m(\varepsilon_{ep}) \tag{22a}$$

$$f_1 = \psi_2(\boldsymbol{\sigma}_B) - \xi\sigma_0^m(\varepsilon_{ep}) \tag{22b}$$

where ε_{ep} is the equivalent plastic strain, and σ_0 is the uniaxial yield stress with isotropic hardening. The Voce's isotropic hardening law and hardening modulus H is given by

$$\sigma_0 = A - B \cdot exp\left(-\varepsilon_{ep} \cdot C\right) \tag{23}$$

$$H = \frac{\partial\sigma_0}{\partial\varepsilon_{ep}} = B \cdot C \cdot exp\left(-\varepsilon_{ep} \cdot C\right) \tag{24}$$

where A, B, and C are the material constant. If $f_1 \le 0$, the material is in its elastic state ($\Delta\boldsymbol{\varepsilon}^p = 0$) and the stress is updated by

$$\boldsymbol{\sigma} = \boldsymbol{\sigma} + \mathbf{D} : \Delta\boldsymbol{\varepsilon}^t \tag{25}$$

If $f_1 > 0$, the material is in its plastic state and the constitutive model provides a suitable set of algorithms for stress integration in the non-linear finite element analysis. Unconditional stability integration of the constitutive model is achieved using the backward-Euler algorithm (Fig. 4) [27]. In the backward-Euler algorithm, an associated plastic flow rule is employed. This rule assumes the plastic strain rate is normal to the yield surface and expressed as

$$\Delta\boldsymbol{\varepsilon}^p = \Delta\varepsilon_{ep} \cdot \frac{\partial\sigma_e}{\partial\boldsymbol{\sigma}} = \Delta\varepsilon_{ep} \cdot \mathbf{a} \tag{26}$$

$$\Delta\varepsilon_{ep} = \frac{\boldsymbol{\sigma} : \Delta\boldsymbol{\varepsilon}^p}{\sigma_e} = \frac{\boldsymbol{\sigma} : \dot{\lambda}\mathbf{a}}{\sigma_e} = \frac{\sigma_e\dot{\lambda}}{\sigma_e} = \dot{\lambda} \tag{27}$$

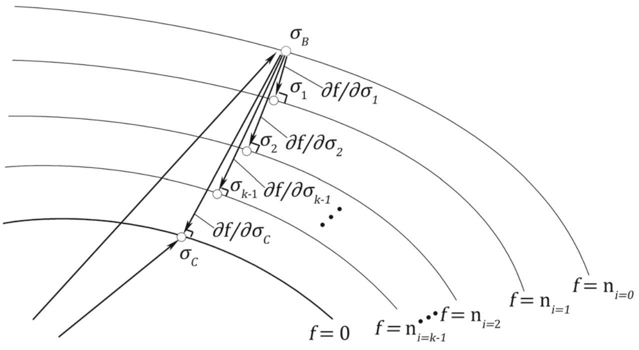

Fig. 4 The backward-Euler single vector return

where $\Delta\boldsymbol{\varepsilon}^p$ is the plastic strain increment, $\Delta\varepsilon_{ep}$ is the equivalent plastic strain increment, and $\dot{\lambda}$ is the plastic strain-rate multiplier. $\mathbf{a} = \frac{\partial\sigma_e}{\partial\boldsymbol{\sigma}}$ is the flow direction calculated by the chain rule:

$$\frac{\partial\sigma_e}{\partial\boldsymbol{\sigma}} = \frac{1}{4m\sigma_e^{(m-1)}}\frac{\partial\psi_1}{\partial\boldsymbol{\sigma}} \tag{28a}$$

$$\frac{\partial\sigma_e}{\partial\boldsymbol{\sigma}} = \frac{1}{\xi m\sigma_e^{(m-1)}}\frac{\partial\psi_2}{\partial\boldsymbol{\sigma}} \tag{28b}$$

where $\frac{\partial\psi_1}{\partial\boldsymbol{\sigma}}$ and $\frac{\partial\psi_2}{\partial\boldsymbol{\sigma}}$ are the first-order derivatives of Yld2004 and new yield function, respectively. Voce's hardening law was incorporated into the Yld2004 and new yield function to form the yield criterion, respectively:

$$f_2 = \psi_1\left(\boldsymbol{\sigma}_{\boldsymbol{C}}\right) - 4\sigma_0^m\left(\varepsilon_{ep} + \Delta\varepsilon_{ep}\right) = 0 \tag{29a}$$

$$f_2 = \psi_2\left(\boldsymbol{\sigma}_{\boldsymbol{C}}\right) - \xi\sigma_0^m\left(\varepsilon_{ep} + \Delta\varepsilon_{ep}\right) = 0 \tag{29b}$$

The corrective plastic stress $\boldsymbol{\sigma}_C$ is given as

$$\boldsymbol{\sigma}_C = \boldsymbol{\sigma}_B - \mathbf{D} : \Delta\boldsymbol{\varepsilon}^p = \boldsymbol{\sigma}_B - \dot{\lambda} \cdot \mathbf{D} : \mathbf{a}_C \tag{30}$$

where $\boldsymbol{a}_C$ is the flow direction of $\boldsymbol{\sigma}_C$ and calculated by Eq. 28 (a and b).

In order to solve for $\boldsymbol{\sigma}_C$, the Newton-Raphson method was employed to reduce the residual vector $\mathbf{r}$ to zero while the final stresses satisfy the yield criterion $f_2 = 0$. The expression for $\mathbf{r}$ is given as:

$$\mathbf{r} = \boldsymbol{\sigma}_C - \left(\boldsymbol{\sigma}_B - \dot{\lambda} \cdot \mathbf{D} : \mathbf{a}_C\right) \tag{31}$$

The initial prediction of corrective stress tensor $\boldsymbol{\sigma}_{C(0)}$, plastic strain-rate multiplier $\dot{\lambda}_{(0)}$, and increment of equivalent plastic strain $\Delta\varepsilon_{ep(0)}$ is given as

$$\dot{\lambda}_{(0)} = \frac{f_1}{\mathbf{a}_B^T : \boldsymbol{D} : \mathbf{a}_B + H} \tag{32}$$

$$\boldsymbol{\sigma}_{C(0)} = \boldsymbol{\sigma}_B - \dot{\lambda}_{(0)} \cdot \boldsymbol{D} : \mathbf{a}_B \tag{33}$$

$$\Delta\varepsilon_{ep(0)} = \dot{\lambda}_{(0)} \tag{34}$$

The iterative change $\Delta\boldsymbol{\sigma}_{C(k+1)}$ and $\Delta\dot{\lambda}_{(k+1)}$ in iteration step $k+1$ are given as:

$$\Delta\boldsymbol{\sigma}_{C(k+1)} = -\mathbf{Q} : \mathbf{r} - \Delta\dot{\lambda} \cdot \mathbf{Q} : \mathbf{D} : \mathbf{a}_C \tag{35}$$

$$\Delta\dot{\lambda}_{(k+1)} = \frac{f_2 - \mathbf{a}_C^T : \mathbf{Q} : \mathbf{r}}{\mathbf{a}_C^T : \mathbf{Q} : \mathbf{D} : \mathbf{a}_C + H} \tag{36}$$

where the $\mathbf{Q}$ is given by

$$\mathbf{Q} = -\left(\mathbf{I} + \dot{\lambda} \cdot \mathbf{D} : \mathbf{P}_C\right)^{-1} \tag{37}$$

where $\mathbf{I}$ is the identity matrix and the second-order derivatives $\mathbf{P} = \frac{\partial^2\sigma_e}{\partial\boldsymbol{\sigma}\partial\boldsymbol{\sigma}}$ for the effective stress which is given by the chain rule, where $\frac{\partial^2\psi_1}{\partial\boldsymbol{\sigma}\partial\boldsymbol{\sigma}}$ and $\frac{\partial^2\psi_2}{\partial\boldsymbol{\sigma}\partial\boldsymbol{\sigma}}$ are the second-order derivatives of Yld2004 and new yield function, respectively:

$$\frac{\partial^2\sigma_e}{\partial\boldsymbol{\sigma}\partial\boldsymbol{\sigma}} = \frac{1}{4m\sigma_e^{(m-1)}}\left(\frac{\partial^2\psi_1}{\partial\boldsymbol{\sigma}\partial\boldsymbol{\sigma}} - \frac{m-1}{4m\sigma_e^m}\frac{\partial\psi_1}{\partial\boldsymbol{\sigma}}\otimes\frac{\partial\psi_1}{\partial\boldsymbol{\sigma}}\right) \quad (38a)$$

$$\frac{\partial^2\sigma_e}{\partial\boldsymbol{\sigma}\partial\boldsymbol{\sigma}} = \frac{1}{\xi m\sigma_e^{(m-1)}}\left(\frac{\partial^2\psi_2}{\partial\boldsymbol{\sigma}\partial\boldsymbol{\sigma}} - \frac{m-1}{\xi m\sigma_e^m}\frac{\partial\psi_2}{\partial\boldsymbol{\sigma}}\otimes\frac{\partial\psi_2}{\partial\boldsymbol{\sigma}}\right) \quad (38b)$$

Corrective stress, plastic strain-rate multiplier, and equivalent plastic strain increment are updated in the iterative process:

$$\boldsymbol{\sigma}_{C(k+1)} = \boldsymbol{\sigma}_{C(k)} + \Delta\boldsymbol{\sigma}_{C(k+1)} \quad (39)$$

$$\dot{\lambda}_{(k+1)} = \dot{\lambda}_{(k)} + \Delta\dot{\lambda}_{(k+1)} \quad (40)$$

$$\Delta\varepsilon_{ep(k+1)} = \dot{\lambda}_{(k+1)} \quad (41)$$

Finally, the Jacobian matrix $\mathbf{D}_{ct}$ in the plastic state was employed to update the plastic stress and can be defined as

$$\mathbf{D}_{ct} = \left(\mathbf{R} - \frac{\mathbf{R}:\mathbf{a}:\mathbf{a}^T:\mathbf{R}}{\mathbf{a}^T:\mathbf{R}:\mathbf{a}+H}\right) \quad (42)$$

$$\boldsymbol{\sigma} = \boldsymbol{\sigma} + \mathbf{D}_{ct} : \Delta\boldsymbol{\varepsilon}^t \quad (43)$$

where the $\mathbf{R} = \mathbf{Q} : \mathbf{D}$. Figure 5 shows the flow diagram of the new constitutive model which has been coded in UMAT and implemented in ABAQUS 6.14-1.

2.4 Deep drawing and redrawing : experiments and models

Two sets of experiments were performed for the deep drawing process and for the redrawing process. In the first set, three cups were deep drawn. Round blanks (radius R_b = 69.41 mm and thickness t = 0.25 mm) were cut from the as-rolled sheet, then fed into the deep drawing tooling (with lubricant) to form a 44.74-mm radius cup. In the second set of experiments, these three deep-drawn cups were fed into the redrawing tooling to form 33-mm radius cups. The earing profiles of the deep-drawn and redrawn cups were measured (using Erichsen Ear Measuring Instrument) and the results were used to validate the accuracy of FE predictions. The geometry and dimensions of the tooling system of deep drawing and redrawing for AA3104-H19 cup used in this study are given in Table 2.

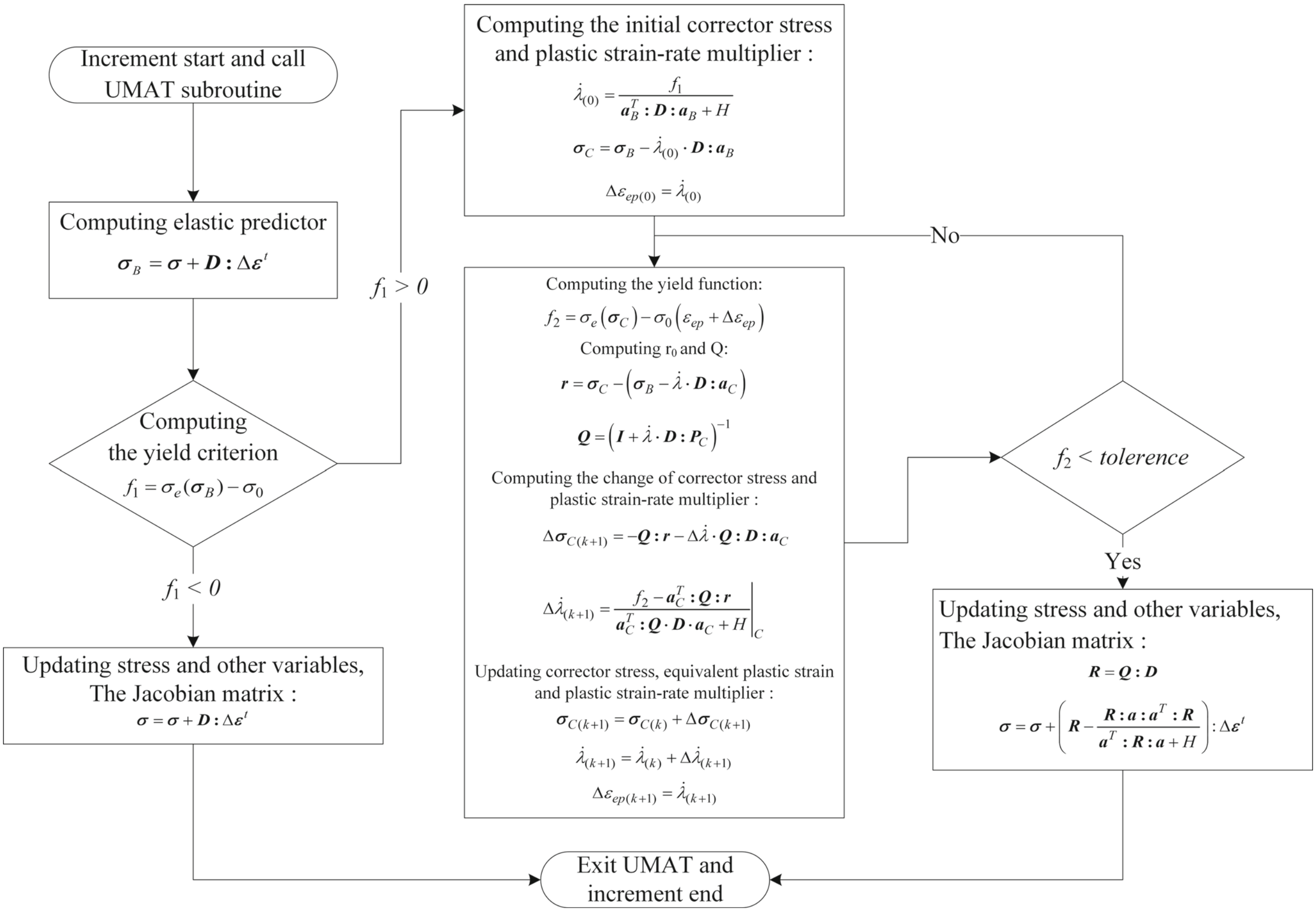

Fig. 5 A flow diagram of the backward-Euler return algorithm for the new constitutive model

Table 2 Parameters of tooling system (units are mm)

Deep drawing		Redrawing	
Die opening diameter D_1	89.78	Die opening diameter D_3	67.40
Punch diameter D_2	89.18	Punch diameter D_4	66.00
Punch profile radius R_1	3.14	Blank holder diameter D_5	85.00
Holder profile radius R_2	5.00	Die profile radius R_4	3.00
Die profile radius R_3	5.00		

The constitutive model for anisotropic sheet metal and the stress integration algorithms (Section 2.3) were coded and the consistent tangent modular is computed to achieve quadratic convergence in the solution process. The forming process was treated as a static problem; therefore, the implicit solver ABAQUS/Standard was employed. Plane stress element type S4R (four nodes shell element with reduced integration) was employed for the blank. Punch, blank holder, and dies were assumed to be rigid bodies. Nine integration points (Simpson rule) through the thickness were employed to achieve accurate results including spring-back. Coulomb friction was assumed with a coefficient $\mu = 0.03$. The stress-strain curve given by Voce's hardening law $\sigma_0 = 329.10 - 52.59 \cdot exp\left(-\varepsilon_{ep} \cdot 39.23\right)$ was employed in FE code to describe constitutive behaviour of AA3104-H19 sheet metal.

Figure 6 shows a cross-section of a circular cup deep drawing process. The deep drawing process is modelled in six steps given by

- Application of 20 kN blank-holder force to avoid flange wrinkling.
- Initial intermediate deep drawing stroke of 27 mm.
- Reducing the blank-holder force to 6 kN.
- Continue deep drawing to complete the stroke.
- Releasing all constraints (punch and blank holder action) to allow spring-back of the deep-drawn cup.

The next redrawing process further reduces the cup diameter and increases the height of deep-drawn cup (Fig. 7). The combination of deep drawing and redrawing are performed to avoid fracture associated with high strain ratio in a single forming process. As expected, the variation of earing profile is increased after the redrawing process. Therefore, it is important to accurately predict the earing profile that develops after both deep drawing and redrawing. The redrawing process consists of seven steps given by

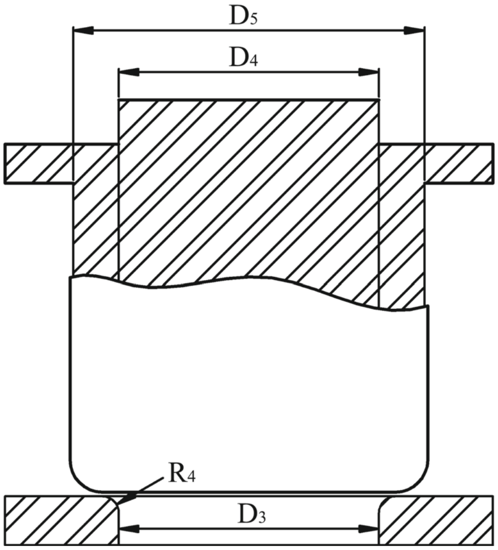

Fig. 7 Circular cup redrawing process

- Feeding the drawn cup into the redrawing tooling.
- Applying the 10-kN blank-holder force on the drawn cup.
- Initial intermediate redrawing stroke of 56 mm.
- Reducing the blank-holder force to 3 kN.
- Continue deep drawing to complete the stroke.
- Releasing all constraints (punch and blank holder action) to allow spring-back of the redrawn cup.

2.5 Optimisation of non-round blank shape

The conventional direct inversing optimisation approach (Eqs. 44–46) makes use of a perfectly round blank (radius R^{RT}) as a starting point. The FE model is used to predict the resultant earing profile $H^{RT}(\varphi)$ after redrawing. The

Fig. 6 Cross-section of circular cup deep drawing process

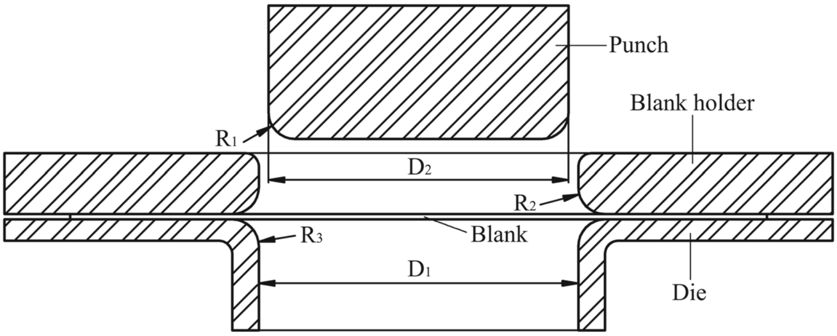

mismatch between the earing profile $H_{k-1}^{NRT}(\varphi)$ generated by the blank shape $R_{k-1}^{NRT}(\varphi)$ (in the previous iteration step) and an ideal ear-free cup height H_{Tgt} is measured from the centre point of the blank and used to offset the radial length to estimate the next improved non-round blank profile $R_k^{NRT}(\varphi)$.

$$R_0^{NRT}(\varphi) = R^{RT} \tag{44}$$

$$H_0^{NRT}(\varphi) = H^{RT}(\varphi) \tag{45}$$

$$R_k^{NRT}(\varphi) = H_{Tgt} - H_{k-1}^{NRT}(\varphi) + R_{k-1}^{NRT}(\varphi) \tag{46}$$

The iteration continues until the difference between the maximum and minimum cup heights satisfies the condition for a prescribed tolerance (tol):

$$f = max\left(H_k^{NRT}(\varphi)\right) - min\left(H_k^{NRT}(\varphi)\right) < tol \tag{47}$$

This conventional approach generally works for deep drawing; however, in the case of redrawing, the strain ratios are much higher leading to poor estimation of subsequent profiles and poor convergence of the solution in the iterative process. The radial length offset applied to the non-round blank as a starting profile is shown in Fig. 8 but the iterative process was not able to converge with the conventional direct inversing approach as shown by the eating profile after the first and second iteration (Fig. 9).

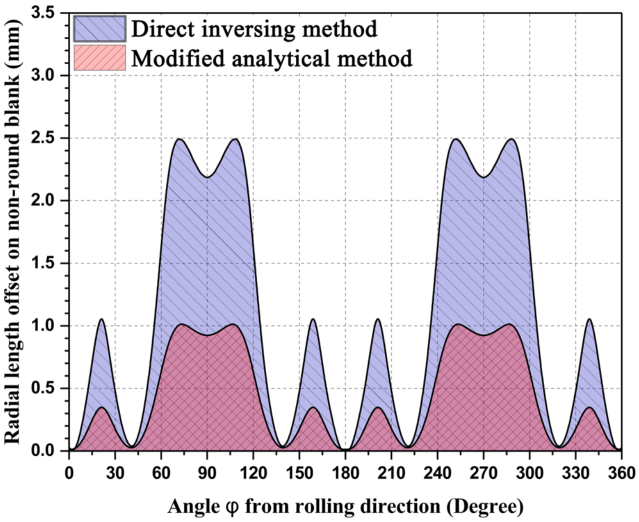

Fig. 8 The radial length offset applied to the non-round blank as a starting profile using conventional direct inversing method and the modified method

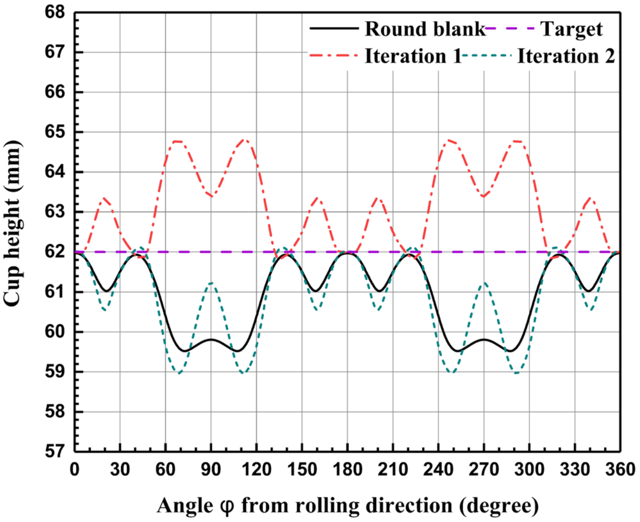

Fig. 9 The predicted earing profiles after the first and second iterations using conventional direct inversing method and the target ear-free profile (cup height = 62 mm)

Here, this problem is resolved by modifying an analytical method [28] to give an improved estimated non-round blank shape. In this analytical calculation, the radial strains of different radial length from rolling direction to transverse direction in the flange zone are given by

$$\varepsilon_r(R,\varphi) = ln\left(B_\varphi \frac{R}{R_c}\right)^{A_{\varphi+\pi/2}} \tag{48}$$

where,

$$A_{\varphi+\pi/2} = \frac{r_{\varphi+\pi/2}}{1 + r_{\varphi+\pi/2}} \tag{49}$$

$$B_\varphi = \left(\frac{\sigma_{ref}}{\sigma_\varphi^Y}\right)^{\frac{1}{2}} \tag{50}$$

$$\sigma_{ref} = \frac{\int_0^{2\pi} \sigma_\varphi^Y d\varphi}{2\pi} \tag{51}$$

where R is the radial length in the flange zone and $R_c = \frac{D_3}{2}$ is the redrawn die opening radius. $r_{\varphi+\pi/2}$ is the directional r-value in the angle $\varphi+\pi/2$ from rolling direction calculated by Eq. 16. σ_φ^Y is the directional yield stress in the angle φ from rolling direction calculated by Eq. 14 .

The cup height can be obtained by integrating the radial strains through the flange zone (Fig. 10 and defined as

$$H_{cup}(\varphi) = t_0 + r_c + \int_{R_c}^{R_b} exp[\varepsilon_r(R,\varphi)]dR \tag{52}$$

where the t_0 is the initial blank thickness and r_c is the punch profile radius. R_b is the radial length of the blank.

The blank of a cup can be viewed as a ring (Fig. 10) with the inner edge drawn into the inside cavity under uniform displacement boundary control. When the ring starts to draw in, different levels of compressive strains are generated circumferentially due to planar anisotropy. The

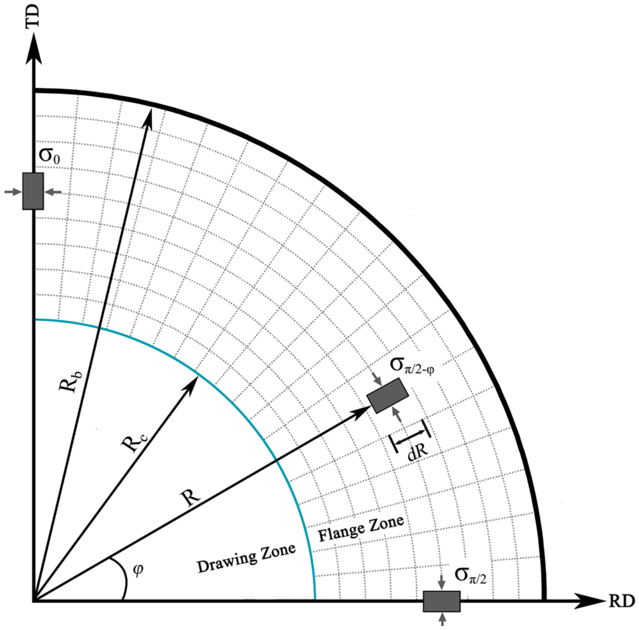

Fig. 10 The circumferential strain at the flange area of the initial blank under simple compression shown in a quadrant from rolling direction (RD) to transverse direction (TD)

corresponding radial strains contributing to the cup height profile (earing profile) result from the incompressibility condition under a plane stress state. Therefore, this non-round blank optimisation method is based on the analytical radial strain which was used to calculate the deformation or offset in the radial length. Hence, for a high strain ratio redrawing process, the offset radial length on the non-round blank predicted by this approach provides better estimates for each iteration which promotes convergence of the solution.

The dimensions of the non-round blank of every iteration process are given by

$$\lambda\left(H_{Tgt} - H_{k-1}^{NRT}(\varphi)\right) = H_{k}^{NRT}(\varphi) - H_{k-1}^{NRT}(\varphi) \\ = \int_{R_c}^{R_k^{NRT}(\varphi)} exp[\varepsilon_r(R,\varphi)]dR - \int_{R_c}^{R_{k-1}^{NRT}(\varphi)} exp[\varepsilon_r(R,\varphi)]dR \tag{53}$$

Therefore, the blank profile or shape after iteration can be defined as

$$R_k^{NRT}(\varphi) \\ = \left[\frac{\lambda\left(H_{Tgt} - H_{k-1}^{NRT}(\varphi)\right)(A_{\varphi+\pi/2}+1)R_c^{A_{\varphi+\pi/2}}}{B_{\varphi}^{A_{\varphi+\pi/2}}} \right. \\ \left. + R_{k-1}^{NRT}(\varphi)^{A_{\varphi+\pi/2}+1}\right]^{\frac{1}{A_{\varphi+\pi/2}+1}} \tag{54}$$

where the λ ($0 < \lambda < 1$) is the multiple which was used to control the size of the increment in the iteration process. Increasing λ causes the iterations to converge quickly but if λ is too large, it may cause poor convergence. Small λ ensure the iterations to converge but as expected would increase the iteration times. In this paper, the λ was selected as 0.5 which resulted in good convergence. The radial length offset on the non-round blank in the starting point using the modified analytical method is shown in Fig. 8. The modified

Fig. 11 Iteration optimisation process of determination of ear-free redrawn cup by using conventional direct inversing method and modified analytical method, respectively

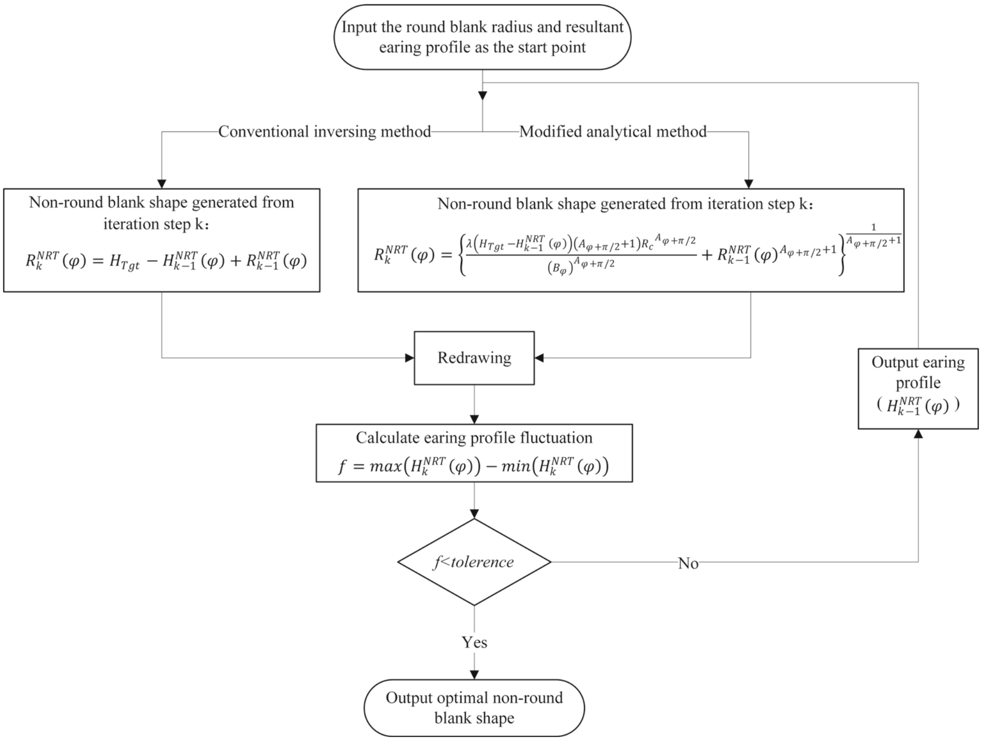

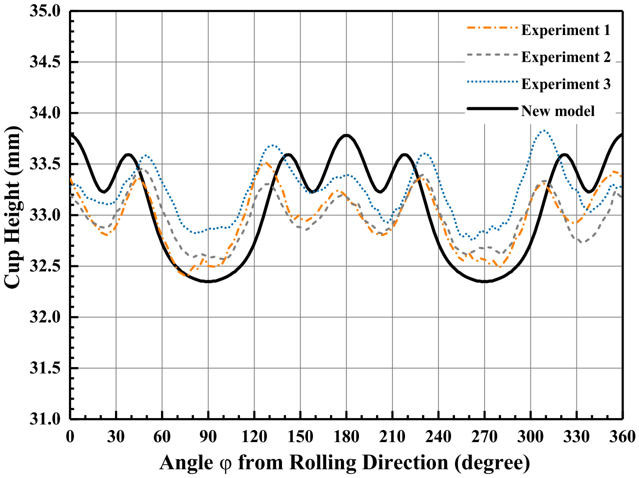

Fig. 12 Comparison between predicted (new model) and measured earing profiles of deep-drawn cups (round blank)

iteration optimisation approach is obtained by replacing Eq. 46 with Eq. 54. Figure 11 shows a flow chart to illustrate the modified analytical and conventional direct inversing non-round blank shape optimisation method, respectively.

3 Results and discussion

Figure 12 shows cup heights or earing profiles (using round blanks) of experimental deep-drawn cups and those predicted by the FE model. The experimental deep-drawn cups show six major ears at 0°, 50°, 130°, 180°, 230°, and 310° and two minor ears in 90° and 270° (with respect to the rolling direction). The model accurately predicts the general profile of the six major ears which is in good agreement with the experimental results. The two minor ears are just noticeable in the experimental results but are too small to be seen in the predicted results. Figure 13 shows experimental and predicted cup heights by respectively adopting the Yld2004 and new yield function after redrawing (round blank). The experimental redrawn cups show six major ears at 0°, 50°, 130°, 180°, 230°, and 310° and two minor ears in 90° and 270° (with respect to the rolling direction). As expected, the heights of the ears are more prominent after redrawing and the new model accurately predicts both the general profile of the six major ears as well as the two minor ears which agrees better with experimental results compared with the Yld2004 yield function.

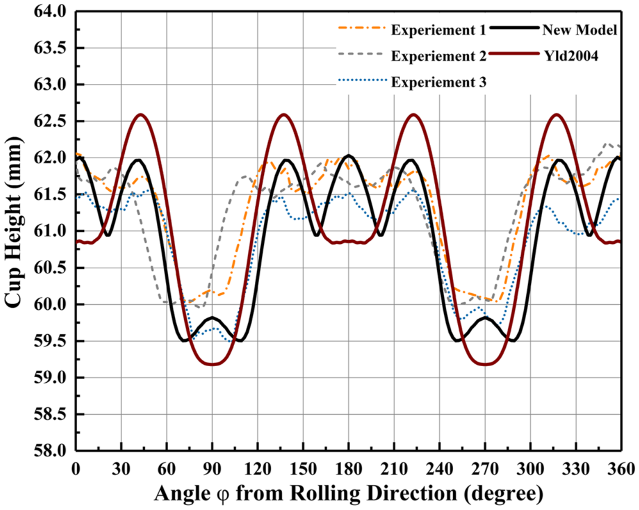

Fig. 13 Comparison between predicted (new model and Yld2004) and measured earing profiles of redrawn cups (round blank)

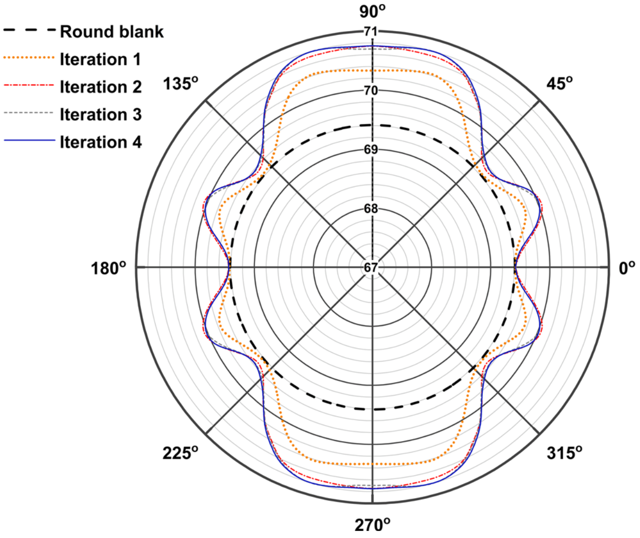

Fig. 14 The development of the blank shape in the iterative process for determination of ear-free redrawn cup using the modified analytical approach

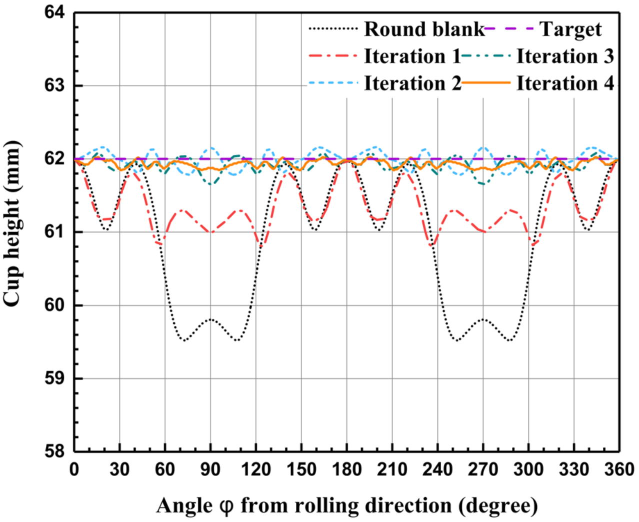

Fig. 15 The development of earing profile in the iterative process for determination of ear-free redrawn cup using the modified analytical approach

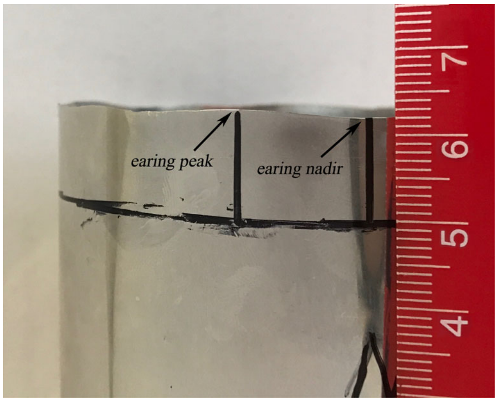

Fig. 16 The experimental redrawn cup formed using the optimal non-round blank

The method described in Section 2.5 was employed to determine the non-round blank profiles that will result in ear-free redrawn cups. Here, the target cup height set was set to 62 mm and convergence threshold was set to 0.2 mm. Convergence was quickly achieved after the fourth iteration by this modified approach which provides better estimates for the radial strain at the start of each iteration. The optimal blank shape which resulted in ear-free redrawn cup along with the intermediate non-round blanks and the corresponding cup heights (earing profile) for each iteration is shown in Figs. 14 and 15. The numerical optimisation results show the earing level (difference between the maximum and minimum cup heights) of the optimal blank shape was significantly reduced to 0.16 mm compared to 2.5 mm with the conventional round blank. The optimal blank shape was used in the experimental forming processes and the experimental redrawn cup formed using this optimal blank shape is shown in Fig. 16. In the experiments, the earing level of the redrawn cup using the optimal blank shape was reduced to 0.7 mm compared to the earing level of 2.3 mm in experiments using the conventional round blank.

In can making, high earing levels frequently contribute to jams in either deep drawing, redrawing, or ironing processes. Most studies undertaken to date have focussed on developing non-round profiles that give low or ear-free cups after deep drawing. Although the shape of a non-round blank has been optimised to give ear-free deep-drawn

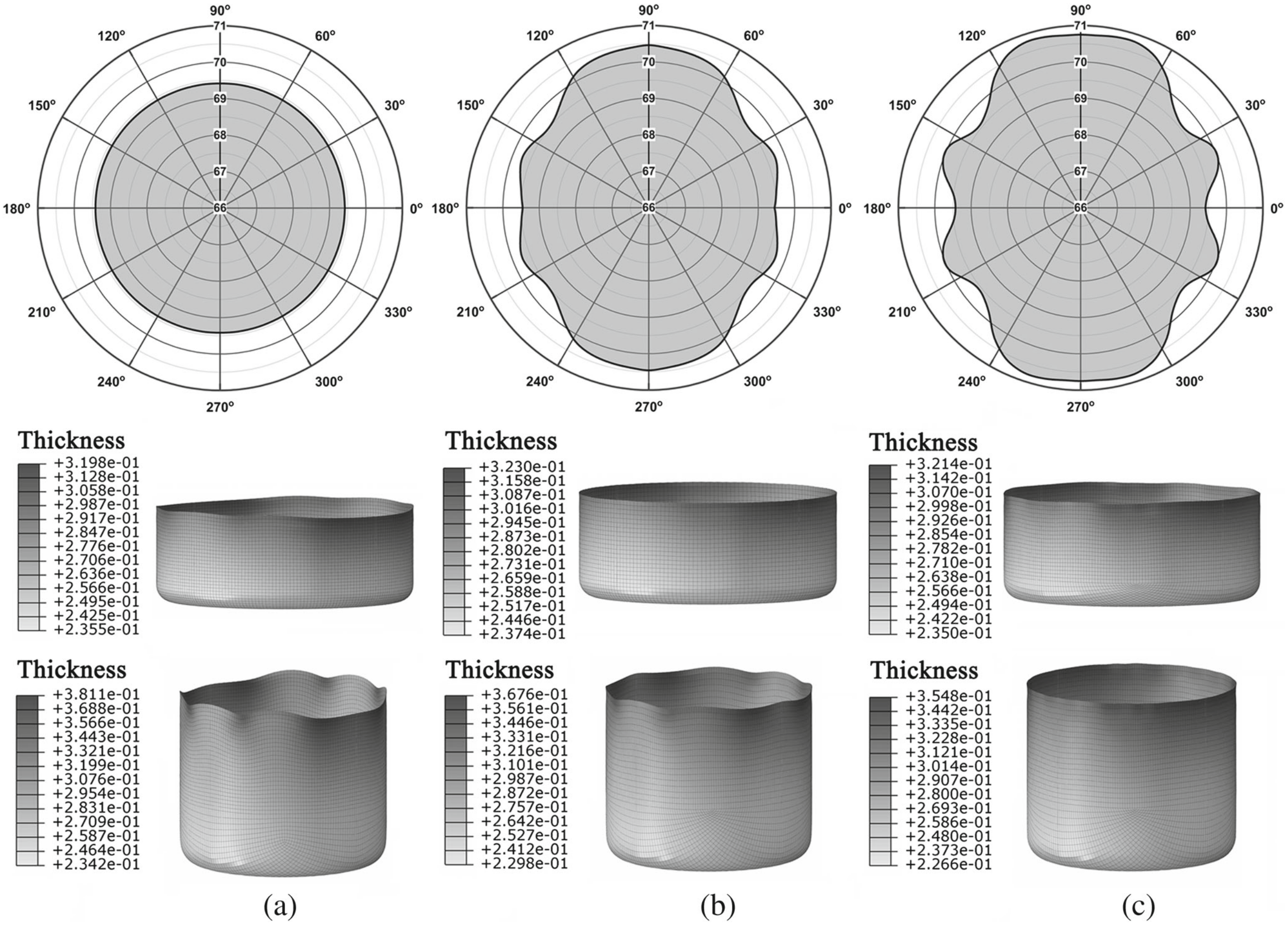

(a) (b) (c)

Fig. 17 Comparison of **a** conventional round blank, **b** optimal non-round blank resulting in ear-free deep-drawn cup, and **c** optimal non-round blank resulting in ear-free redrawn cup in the multi-step forming process cup, earing continues to develop in the redrawing process which may still lead to the jams in the ironing process. Therefore, this work shows that non-round blank profiles should aim to achieve minimum levels of earing after a combination of the deep drawing and redrawing process to ensure earing levels are minimised in the ironing process [20]. Figure 17b, c shows the non-round blank profiles optimised to give minimum earing after deep drawing and redrawing, respectively.

Ideally, the anisotropic deformation that takes place during ironing should also be thoroughly considered so that excessive earing does not contribute to disruptions in this extremely high strain and precise forming process. Also, low levels of earing in the finished ironed can bodies would promote better utilisation of material. Both experimental and numerical investigations are continuing to develop non-round blank profiles that are optimised for the three combined processes: deep drawing, redrawing, and ironing.

4 Conclusions

i. A new anisotropic yield function which accurately describes the complex anisotropy of AA3104-H19 aluminium alloy sheet metal was proposed and applied to determine the optimal shape of the initial non-round blank to obtain the ear-free redrawn cups.
ii. A non-linear least square method was used to determine the coefficients of this yield function based on experimental results. By employing the back-Euler stress integration algorithm, this new anisotropic constitutive model has been successfully implemented in commercial FEM software ABAQUS via user material subroutine UMAT to predict earing profile of AA3104-H19 deep-drawn cups and redrawn cups.
iii. Good agreement was found in the predicted earing profiles and those obtained in experimental cups deep drawn and redrawn using conventional round tooling.
iv. Results showed the level of the final earing is significantly reduced in the redrawn cup using optimal non-round blank shape compared with the conventional round blank. Eliminating or reducing the level of earing in redrawn cups is vital for smooth running of the high-speed can body manufacturing process.
v. The anisotropic yield model is presented in a general form which can be readily adapted for other aluminium alloys used in sheet forming applications such as in net shape forming of automotive components.

Acknowledgements The authors are grateful to Mr Mike Shirran for the technical support for this work.

Compliance with ethical standards

Conflict of interest The authors declare that they have no conflict of interest.

References

1. Buffington J (2012) The beverage can in the United States: achieving a 100% recycled aluminium can through supply chain innovation. JOM 64(8):923–932
2. Kanetake N, Tozawa Y, Otani T (1983) Calculations from texture of earing in deep drawing for FCC metal sheets. Int J Mech Sci 25(5):337–345
3. Kao PW (1985) Texture and earing behaviour of cold-rolled aluminium alloy 3004. Mater Sci Eng 74(2):147–157
4. Yu TM, Brooks CR, Goodrich S (1993) The effect of cold working and annealing practice on earing in 3104 Al alloy sheet. Mater Charact 30(4):251–259
5. Jahazi M, Goudarzi M (1997) The influence of thermomechanical parameters on the earing behaviour of 1050 and 1100 aluminium alloys. J Mater Process Technol 63(1-3):610–613
6. Saha R, Ray RK (2007) Microstructural and textural changes in a severely cold rolled boron-added interstitial-free steel. Scr Mater 57(9):841–844
7. Thiruvarudchelvan S, Loh NH (1994) Deep drawing of cylindrical cups with friction-actuated blank holding. J Mater Process Technol 40(3-4):343–358
8. Kitayama S, Natsume S, Yamazaki K, Han J, Uchida H (2016) Numerical investigation and optimization of pulsating and variable blank holder force for identification of formability window for deep drawing of cylindrical cup. Int J Adv Manuf Technol 82(1-4):583–593
9. Kitayama S, Natsume S, Yamazaki K, Han J, Uchida H (2015) Numerical optimization of blank shape considering flatness and variable blank holder force for cylindrical cup deep drawing. Int J Adv Manuf Technol
10. Pegada V, Chun Y, Santhanam S (2002) An algorithm for determining the optimal blank shape for the deep drawing of aluminum cups. J Mater Process Technol 125:743–750
11. Wang J, Goel A, Yang F, Gau JT (2009) Blank optimization for sheet metal forming using multi-step finite element simulations. Int J Adv Manuf Technol 40(7):709–720
12. Naceur H, Guo YQ, Batoz JL (2004) Blank optimization in sheet metal forming using an evolutionary algorithm. J Mater Process Technol 151(1):183–191
13. Chung K, Barlat F, Brem JC, Lege DJ, Richmond O (1997) Blank shape design for a planar anisotropic sheet based on ideal forming design theory and FEM analysis. Int J Mech Sci 39(1):105–120
14. Vafaeesefat A (2011) Finite element simulation for blank shape optimization in sheet metal forming. Mater Manuf Process 26(1):93–98
15. Kishor N, Kumar DR (2002) Optimization of initial blank shape to minimize earing in deep drawing using finite element method. J Mater Process Technol 130:20–30
16. Hino R, Yoshida F, Toropov VV (2006) Optimum blank design for sheet metal forming based on the interaction of high- and low-fidelity FE models. Arch Appl Mech 75(10):679–691
17. Park SH, Yoon JW, Yang DY, Kim YH (1999) Optimum blank design in sheet metal forming by the deformation path iteration method. Int J Mech Sci 41(10):1217–1232

18. Barlat F, Lian K (1989) Plastic behaviour and stretchability of sheet metals. Part I: a yield function for orthotropic sheets under plane stress conditions. Int J Plast 5.1:51–66
19. Engler O, Norbert M, Pim VD (2011) Texture-based design of a convoluted cut-edge for earing-free beverage cans. J Mater Process Technol 211.7:1278–1284
20. Rkas A, Latos T, Budzyn R, Fijakowski M, Brodawka L (2015) The analysis of influence of sheet properties on the ironing process of thin-walled cylindrical shell products from aluminium alloys. Key Engng Mater 641:232–245
21. Barlat F, Brem JC, Yoon JW, Chung K, Dick RE, Lege DJ, Chu E (2003) Plane stress yield function for aluminium alloy sheets—part 1: theory. Int J Plast 19.9:1297–1319
22. Yoon JW, Barlat F, Dick RE, Chung K, Kang TJ (2004) Plane stress yield function for aluminium alloy sheets—part II: FE formulation and its implementation. Int J Plast 20.3:495–522
23. Barlat F, Aretz H, Yoon JW, Karabin ME, Brem JC, Dick RE (2005) Linear transformation-based anisotropic yield functions. Int J Plast 21.5:1009–1039
24. Yoon JW, Barlat F, Dick RE, Karabin ME (2006) Prediction of six or eight ears in a drawn cup based on a new anisotropic yield function. Int J Plast 22(1):174–193
25. Aretz H, Aegerter J, Engler O (2010) Analysis of earing in deep drawn cups. In AIP Conference Proceedings 1252(1):417–424
26. Aretz H, Barlat F (2013) New convex yield functions for orthotropic metal plasticity. Int J Non Linear Mech 51:97–111
27. Crisfield MA, Vincenzo C (1997) Non-linear finite element analysis of solids and structures, vol.1. Meccanica 32(6):586–587
28. Yoon JW, Dick RE, Barlat F (2011) A new analytical theory for earing generated from anisotropic plasticity. Int J Plast 27(8):1165–1184